MIL-100(Fe) MOF as an emerging sulfur-host cathode for ultra long-cycle Metal-Sulfur batteries

Álvaro Bonilla [a,1], Gabriela A. Ortega-Moreno [b,1], María C. Bernini [b], Juan Luis Gómez-Cámer [a], Lucía Isabel Barbosa [b,**], Álvaro Caballero [a,*]

[a] *Dpto. Química Inorgánica e Ingeniería Química, Instituto Químico para La Energía y El Medioambiente (IQUEMA), Universidad de Córdoba, 14014, Córdoba, Spain*
[b] *Instituto de Investigaciones en Tecnología Química (INTEQUI-CONICET), Facultad de Química, Bioquímica y Farmacia, Universidad Nacional de San Luis (UNSL), Almirante Brown 1455, San Luis, 5700, Argentina*

HIGHLIGHTS

- For the first time, Fe-based MOF is used as a sulfur-host in metal-sulfur cathodes.
- MIL-100(Fe) MOF morphology is maintained during electrode preparation process.
- Remarkable rate capability behavior and low polarization are shown by MIL-100(Fe).
- Sulfur/MIL-100(Fe) cathodes overperform other MOFs in Li–S reaching 3000 cycles.
- Highly stable Na–S cathodes are achieved with sulfur/MIL-100(Fe) composites.

GRAPHICAL ABSTRACT
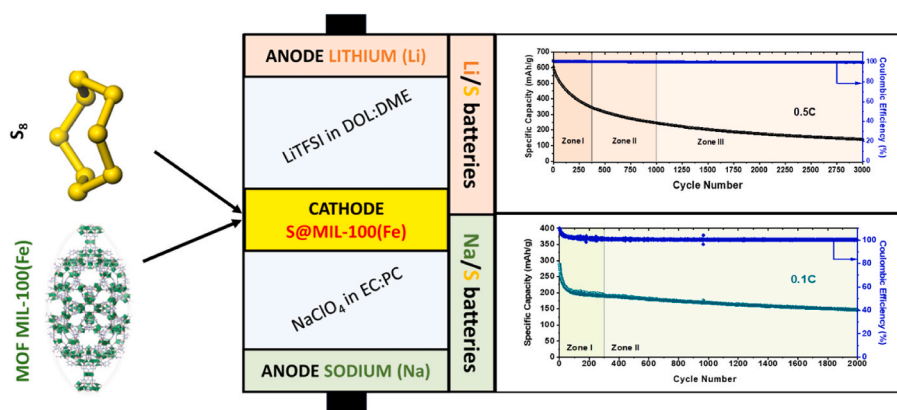
ABSTRACT

Metal–Sulfur (Li/Na–S) battery technology is considered one of the most promising energy storage systems because of its high specific capacity of 1675 mA h/g, attributed to sulfur. However, the rapid capacity degradation, mainly caused by metallic polysulfide dissolution, remains a significant challenge prior to practical applications. This work demonstrates for the first time that a Fe-based metal organic framework (MIL-100(Fe)) can remarkably stabilize the electrochemical behavior of sulfur-cathodes in Metal-S cells during prolonged cycling. The chemical and morphological properties of MIL-100(Fe) and, especially conjugated with their textural characteristics, can help immobilize lithium/sodium polysulfides within the highly microporous cathode structure. Capacity loss per cycle is 0.044 mA h after 3000 cycles at 2C in Li–S cells. This behavior is confirmed when the MOF-based cathode is studied in RT Na–S batteries, managing to stabilize the capacity with a loss of less than 0.08 % during 2000 cycles at 0.1 C-rate. The excellent performance can be attributed to the synergistic

* Corresponding author.
** Corresponding author.
E-mail addresses: lbarbosa@unsl.edu.ar (L.I. Barbosa), alvaro.caballero@uco.es (Á. Caballero).
[1] These authors contributed equally to this work.

effects of the highly microporous structure of MOF-100(Fe), which provide an ideal matrix to confine polysulfides, and the presence of Fe(III) active centers that provide chemical affinities to sulfur and polysulfides. These factors contribute to the excellent cycling performance of the S@MIL-100(Fe) composite in Metal-Sulfur batteries.

1. Introduction

Energy is a pivotal driver of socioeconomic and technological progress, with fossil fuels dominating 83.5 % of the current global energy economy [1,2]. The heavy reliance on oil, coal, and natural gas has led to a surge in atmospheric CO_2 levels, exacerbating global warming and climate change [1]. Recognizing the adverse environmental effects, accelerated by a growing global demand for energy, there is a widespread call for a shift to a low-carbon economy centered on renewable energy sources. These sources have experienced unprecedented growth over the past two decades [3]. However, the inherent challenges of intermittency and fluctuation in renewable energy generation necessitate the integration of energy storage systems (ESS) [4,5]. These systems play a vital role in storing excess electrical energy, ensuring a reliable energy supply during unpredictable generation periods, and optimizing the balance between energy demand and generation for a more sustainable future [3,6]. At present, rechargeable Li-ion batteries (LIBs) stand as the predominant choice for ESS applications [6]. However, LIBs are falling short in addressing the present and future energy requirements of society. For this reason, the attention has turned to the use of batteries based on multielectron redox centers with high energy densities [7–9]. In this respect, Lithium–Sulfur Batteries (LSBs) are emerging as attractive candidates for the development of high-efficiency energy storage systems [8,10] (see Scheme 1).

The key components of LSBs include the following: a cathode consisting of a composite made up of sulfur and a sulfur-host material that store and immobilize the mobile redox centers; an anode made of lithium metal; and an organic electrolyte [9]. These electrochemical devices operate according to the following electrochemical reaction [11]: $16\,Li^+ + S_8 + 16\,e^- \rightleftharpoons 8\,Li_2S; E^0 = 2.15$ V (vs Li/Li^+). With two Li per S atom, LSBs provide a theoretical specific capacity of 1675 mA h/g and a theoretical specific energy of 2600 Wh/kg, which exceeds 3–5 times the theoretical energy supplied by conventional Li-ion systems [9, 11]. In addition, sulfur (S_8) as a conversion cathode material is an abundant element in nature, environmentally sustainable and more economical than current cathode materials including $LiCoO_2$ and $LiFePO_4$ [12].

Although LSBs offer considerable advantages compared to LIBs, they suffer from a drawback associated with the process known as *shuttle*

effect caused by lithium polysulfides (LPSs). This effect leads to sulfur loss, corrosion of the lithium anode, and self-discharge [9,11,13]. To solve such problems, four approaches have been applied [14]: (1) designing new sulfur-host materials capable of trapping polysulfides by physical adsorption and/or chemical bonding [15,16]; (2) modifying separators using functional materials to block the diffusion of polysulfides from the cathode to the anode [17,18]; (3) implementing strategies for lithium-anode protection [19]; and (4) developing new electrolyte systems to limit the migration of polysulfides [20,21].

While the advancement of LSBs technology is influenced by the development of each of these approaches, designing new sulfur-host materials has demonstrated the most significant progress. Porous materials have been widely explored as sulfur-hosts in LSBs cathodes because Li_2S_x species tend to get adsorbed into the porous systems by physical/chemical interactions, reducing the *shuttle effect* [15]. Among the diverse range of porous materials suitable for serving as sulfur-hosts in LSB cathodes, metal-organic frameworks (MOFs) have received considerable attention due to their singular features [9,11,13,22,23]. These strategies can also be effectively applied in Metal-Sulfur technologies, with special interest in Sodium–Sulfur (RT Na–S) batteries due to the inherent advantages offered by sodium, such us low cost, abundance, and environmental friendliness [24,25]. Many strategies have been used to inhibit the *shuttle effect* in sulfur electrodes, encompassing physical, chemical, or electrocatalytic approaches [26]. The present work proposes a combined physical and chemical inhibition strategy, capitalizing on the microporosity and Lewis acid-base interactions, respectively, provided by a pristine MOF. MOFs are crystalline solids formed by the assembly of multifunctional organic ligands and metal centers into a periodic 2D or 3D framework structure characterized by its permanent porosity [27,28]. Compared to other porous materials, MOFs boasts several advantages, including high specific surface area, large pore volume, tunable reactivity derived from their functional groups, and uniformly dispersed metal centers. In some cases, these centers can transform into coordinatively unsaturated metal sites (CUSs) [15,27,28]. The CUSs are active sites capable of accepting electron pairs, functioning as Lewis acids [29], and can even exhibit redox properties [30]. Due to their Lewis acidity, CUSs tend to interact strongly with soluble polysulfides, which are species characterized by their Lewis basicity [31,32]. As a result, the CUSs generated within the MOF
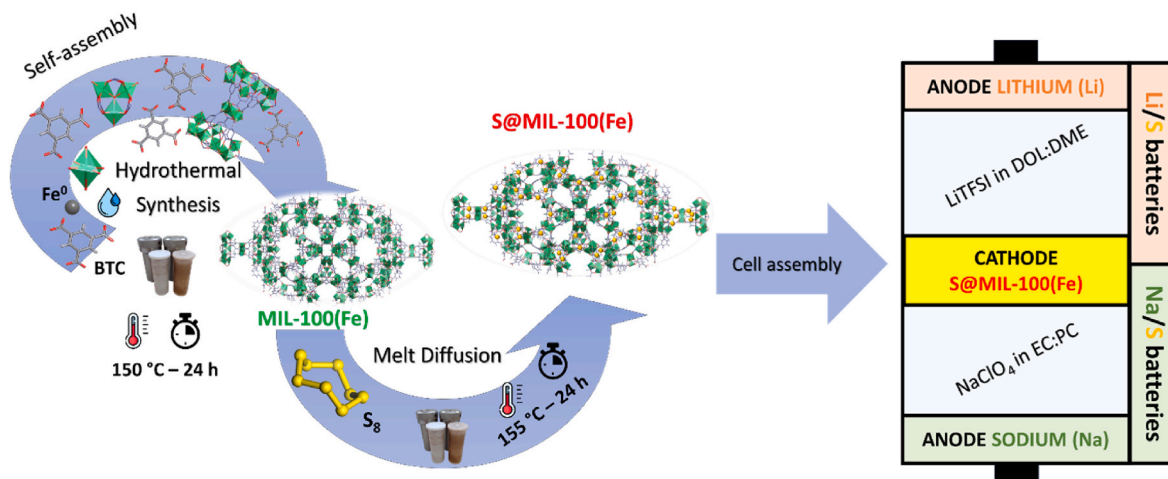
Scheme 1. Scheme for preparation of Metal-Sulfur batteries using MIL-100(Fe) as cathode material.

structure tend to effectively trap soluble polysulfides, significantly slowing down the migration of these species away from the cathode [31, 32] and thus preventing sulfur loss. Therefore, the use of MOFs as sulfur-hosts could provide both an intelligent pore structure and Lewis acid-base interactions, thereby significantly improving the cycling stability of Li–S batteries [32].

Different MOFs have been evaluated as sulfur-host materials for cathodes in Li–S technology. For example, Zhou et al. [9] studied the performance of four MOFs as sulfur hosts: ZIF-8, HKUST-1, NH$_2$-MIL-53 (Al), and MIL-53(Al). The corresponding S@MOF composites were subjected to cycling tests at a constant discharge/charge rate of 0.5 C, achieving capacities of 553, 286, 332 and 347 mA h/g after 300 cycles, respectively. This research has shown that properties of MOFs, such as the Lewis acidity of the CUSs and the size and shape of the cavities/windows, have a profound impact on the electrochemical performance of the composite cathode material [10]. Recently, MIL-88A(Fe) MOF was evaluated as a sulfur-host material in LSB cathodes [11]. The S@MIL-88A(Fe) composite showed excellent cycling stability as a cathode material, delivering an average specific capacity of 300 mA h/g after 1000 cycles [11]. MIL-88A(Fe) features a three-dimensional flexible crystalline structure composed of oxo-centered trinuclear iron(III) clusters, commonly referred to as primary building units (PBUs) [33,34]. These PBUs are characterized by three labile ligands: two water molecules and an anionic specie. Controlled thermal removal of these ligands leads to the formation of two distinct types of CUSs with varying levels of Lewis acidity: Fe^{III} CUSs and Fe^{II} CUSs [35–37]. The presence of these active sites has been linked to long-term cycling stability.

MIL-100 MOFs with different metal centers have been used as sulfur matrices in LSBs. Specifically, MIL-100(V) [13], MIL-100(Cr) [23] and Mn-MIL-100 [38] have demonstrated capacities of 550, 420 and 346 mA h/g, respectively, at a rate of 0.1C after 200 cycles for MIL-100(V) and Mn-MIL-100, and 60 cycles MIL-100(Cr). In this study, we assessed the potential of MIL-100(Fe) MOF as a novel sulfur-host material in Metal-Sulfur cells. MIL-100(Fe) has distinctive features; it has a bimodal mesoporous system [23,32] and PBUs similar in structure to those of MIL-88A(Fe) [35,39], which enables the formation of Fe^{III} CUSs through controlled thermal activation [35]. The present work demonstrates, for the first time, that MIL-100(Fe), containing Fe^{III} CUSs and an ultra-high specific surface area, can provide notable performance in capacity retention in Li–S cells. Furthermore, the behavior of this same S@MIL-100(Fe) composite proves remarkable when tested as a long-cycling cathode in the novel RT Na–S battery technology. Specifically, the use of CUS engineering principles [40] combined with the pore confinement effect constituted a strategy that enhanced the long-term cyclic stability of the cathode when MIL-100(Fe) served as the sulfur-host. This represents progress towards the systematic design of sulfur-host cathodes for long-cycle metal-sulfur batteries.

2. Experimental section

2.1. Materials

Materials used in the experimental section were 1,3,5-benzenetricarboxylic acid (H$_3$BTC; 98 %, Sigma-Aldrich), iron metal (Fe^0; 95 %, BDH Chemicals), hydrofluoric acid (HF; 40 %, Biopack), nitric acid (HNO$_3$; 65 %, Cicarelli), ethanol (CH$_3$CH$_2$OH; 99.5 %, Cicarelli), sulfur (S, Merck), polyvinylidene fluoride (PVDF, Sigma-Aldrich), Super P carbon (SPC, Timcal) and *N*-methyl-2-pyrrolidone (NMP, Sigma-Aldrich), lithium bis-trifluoromethanesulfonylimide, (LiTFSI; 99 %, Solvay), lithium nitrate (LiNO$_3$; 99.9 %, Sigma-Aldrich), 1,2-dimethoxyethane (DME; 99.9 %, Sigma-Aldrich) and 1,3- dioxolane (DOL; 99.8 %, Sigma-Aldrich), sodium perchlorate, anhydrous (NaClO$_4$; 99.99 %, Stem Chemicals), ethylene carbonate (EC; 99 %, Sigma-Aldrich), propylene carbonate (PC; 99.7 %, Sigma-Aldrich) and lithium sulfide (Li$_2$S; 99 %, Sigma-Aldrich).

2.2. Synthesis MIL-100(Fe)

MIL-100(Fe) was synthesized by a hydrothermal process following experimental conditions described in the literature [35,39,41]. In a typical synthesis process, 0.67 mmol of 1,3,5-benzenetricarboxylic acid, 1 mmol of Fe^0 and 5 mL of H$_2$O were mixed in a Teflon-lined stainless-steel autoclave (25 mL internal volume). Subsequently, 2 mmol of HF and 1.5 mmol of HNO$_3$ were added to the reaction mixture. The autoclave was then sealed and heated at 150 °C for 24 h. After the reaction, the synthesized solid was isolated using a Gelec G-142D centrifuge and purified through a two-step procedure [35] under reflux conditions. In the first step, water served as the solvent, and the system was maintained at 80 °C for 5 h. In the second step, the solid was treated with ethanol at 60 °C for 3 h. The purified solid was recovered by centrifugation, dried under ambient conditions, and subsequently activated through controlled thermal treatment at 120 °C for 12 h under dynamic vacuum. The resulting brown powder, named MIL-100(Fe), was used in the preparation of the sulfur-based composite.

2.3. Preparation of the S@MIL-100(Fe) composite

The S@MIL-100(Fe) composite was prepared using the melt diffusion method, which has recently been identified as the optimal technique for fabricating sulfur-based composites for lithium-sulfur batteries [42]. First, MOF MIL-100(Fe) and sulfur (S$_8$) powders were vacuum-dried in a glass oven (Buchi, B-585). Subsequently, the dried powders were thoroughly mixed in a 1:1 ratio in a glove box (*M*-Braun 150; H$_2$O, O$_2$ < 0.1 ppm) with an inert Ar atmosphere. The resulting mixture was then introduced into a hydrothermal reactor, hermetically sealed with an Ar atmosphere, and heated to 155 °C for 24 h.

2.4. Electrode preparation

Cathodes were prepared by mixing 70 wt% S@MIL-100(Fe), 20 wt% SPC as a conducting agent, and 10 wt% PVDF as a binder in NMP as the solvent to make the electrode mixture. This mixture was then cast onto a conductive current collector using the doctor blade coating technique. The electrodes were subsequently dried in an oven at 50 °C for 24 h. Finally, the electrodes were cut into 12.8 mm diameter discs and further dried at 45 °C for 3 h under vacuum in a glass oven (Buchi, B-585).

2.5. Cell assembly and electrochemical measurements

Metal-Sulfur cells were assembled in a coin cell configuration (CR2032) within an argon-filled glove box (Inert model IL-4GB; H$_2$O, O$_2$ < 0.5 ppm). For the lithium-sulfur batteries, a lithium metal disc (0.6 mm thick and 14 mm diameter) served as the counter and the reference electrode, while a polyethylene disc (Celgard 2400) of 25 μm thickness and 16 mm diameter as the separator. The electrolyte was prepared by dissolving 1 M LiTFSI and 0.4 M LiNO$_3$ in a DOL:DME solvent mixture (1:1, v/v). For the sodium-sulfur batteries, a sodium metal disc (0.8 mm thick and 14 mm diameter) was employed as the counter and the reference electrode, with a glass fiber (GF/F Whatman) separator of 400 μm thickness, 16 mm diameter, and 0.6 μm porosity. The electrolyte was prepared by dissolving 1 M NaClO$_4$ in a EC:PC solvent mixture (1:1, v/ v). All reagents were vacuum-dried before electrolyte preparation, ensuring electrolyte humidity, measured in a Karl Fischer (Metrohm) equipment, was <10 ppm. The volume of electrolyte added was 25 μL per milligram of sulfur.

The electrochemical study was performed by galvanostatic measurements using a potentiostat-galvanostat Neware BTS 4000. For LSBs, a voltage window of 1.7–2.8 V vs Li$^+$/Li was employed, while for RT Na–S batteries, the voltage window was set at 0.8–2.8 V. Current density was calculated based on the theoretical sulfur capacity, with 1C corresponding to 1675 mA/g. Capacities and rates were determined considering the mass of sulfur. Cyclic voltammetry (CV) and electrochemical
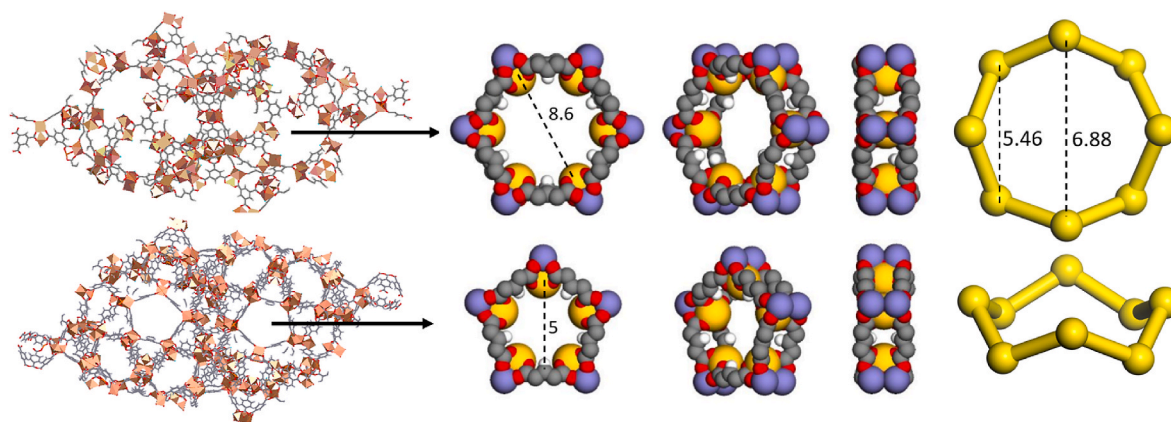
Fig. 1. Left: Projection of the MIL-100 structure showing the mesoporous spherical cavities with pentagonal and hexagonal windows. **Center:** van der Waals representation of different views of the hexagonal and pentagonal windows (the exposed CUSs are highlighted in yellow). **Right:** Detailed dimensions and conformation of S_8. Dashed lines show distances in Angstroms as referenced [45,47]. (For interpretation of the references to color in this figure legend, the reader is referred to the Web version of this article.)

impedance (EIS) measurements were conducted using a potentiostat Pgstat204 (Metrohm Autolab). CV curves were recorded at different scan rates (0.1, 0.2, 0.4, 0.6, 0.8 and 1 mV/s) within a voltage window of 1.5–3.0 V. EIS spectra were measured at open circuit voltage (OCV) and after CV cycles, with frequencies ranging from 500 kHz to 0.005 Hz and a disturbance amplitude of 10 mV. The Zview 2 software by Scribner Associates was used for fitting the equivalent circuit during simulation.

2.6. Polysulfide adsorption tests

Li_2S_6 (0.5 M) was synthesized by mixing Li_2S and sulfur in a 1:5 M ratio and dissolved in a mixture of DOL:DME (1:1, v/v). The solution was stirred at 60 °C for 24 h inside an Ar-filled glovebox to obtain the polysulfide solution. For the polysulfide adsorption test, 20 mg of MIL-100 (Fe), dried under vacuum at 120 °C, were added to a dilute solution of 2 mM Li_2S_6, and the mixture was allowed to rest for 2 h. UV–vis spectra were obtained using 4 mL of supernatant and 4 mL of blank solution (2 mM Li_2S_6) via a double-beam UV/vis 4260/50 ZUZI spectrophotometer.

2.7. Characterization techniques

X-ray Diffraction (XRD) patterns were collected with an Ultima IV type II diffractometer (Rigaku) and a D8 Discover A diffractometer (Bruker) equipped with a LynxEye detector, both utilizing monochromatic Cu-Kα radiation (λ = 1.5418 Å and λ = 1.5406 Å, respectively). Scans were conducted in the 2θ range of 2°–50° with 0.02° increments and a scan rate of 2°/min. Fourier Transform Infrared (FTIR) spectra of the solids were collected using a Nicolet Protégé 460 spectrometer via the KBr pellet technique. Whereas FTIR spectra of the films were recorded on a FTIR-ATR PerkinElmer Spectrum Two. Both experiments covered the 4000–400 cm^{-1} spectral range, with a resolution of 4 cm^{-1} and 40 scans for each sample. Thermogravimetric analyzes (TGA) of MIL-100(Fe) and S@MIL-100(Fe) were performed using a TGA/DSC 1 STAR system (Mettler Toledo) over a temperature range of 25–600 °C, with a ramp of 5 °C/min and a flow rate of 100 mL/min of oxygen or nitrogen, respectively. Raman spectra were measured with an alfa 500 confocal Raman spectrometer (WITec GmbH, Ulm, Germany) using a frequency-doubled Nd:YAG laser (second harmonic generation) at 532 nm for excitation, focused with a 20 × /0.4 Zeiss objective. The Raman spectrum of MIL-100(Fe) was collected using a 600 g/mm diffraction grating and an integration time of 20 s by accumulating a total of 10 spectra and a laser power of 4 mW measured in front of the lens in the range of 400–2000 cm^{-1}. Whereas the Raman spectrum of the S@MIL-100(Fe) composite was collected using a 600 g/mm diffraction grating and an integration time of 10 s by accumulating a total of 10

spectra and a laser power of 1 mW, which was measured before the lens in the range of 100–700 cm^{-1}. X-ray photoelectron spectroscopy (XPS) spectra were collected using a VG Microtech ESCA spectrometer with a non-monochromatic Al K$_\alpha$ radiation source (300 W, 15 kV, hν = 1486.6 eV), combined with a VG-100-AX hemispherical analyzer operating at 25 eV pass energy. The instrumental resolution was 0.1 eV. All the XPS spectra were calibrated with the C 1s peak at 284.6 eV as reference to rule out any possible spectral shift due to charging effects. The chamber pressure was kept at <10^{-9} Torr during the measurements. Data analysis was performed using CasaXPS software. The textural properties of the MIL-100(Fe) and S@MIL-100(Fe) were investigated by N_2 adsorption–desorption isotherms at liquid nitrogen (N_2) temperature (77 K) with a Micromeritics ASAP 2020 system. The specific surface area and the total pore volume of these solids were determined by the Brunauer-Emmett-Teller (BET) method [43] and the Gurvich rule [44] at p/p_0 = 0.98, respectively. The pore size distribution was calculated using the density functional theory (DFT). The morphology of synthesized materials was studied using a LEO1450VP electron microscope equipped with an EDS/EDAX probe for microanalysis, and a JEOL JSM-7800 F with an X-ACT detector. Powdered samples were spread onto sample holders using graphite tape and metallized with a thin layer of gold via sputtering to increase the surface conductivity and prevent calcination due to electron beam irradiation. Additionally, post-mortem SEM images were taken from the electrode of the cell cycled at 0.5C, previously disassembled into a glovebox and immediately washed in a mixture of DOL:DME solvents and put into a vacuum glass oven at 50 °C for 72 h.

3. Results and discussion

3.1. Characterization of MIL-100(Fe)

The MIL-100(Fe) is a rigid MOF composed by oxo-centered trinuclear Fe(III) clusters and 1,3,5-benzenetricarboxylate (BTC^{3-}) as the ligand [41,45,46]. This MOF has two different mesoporous spherical cages, with approximate diameters of 25 and 29 Å, interconnected by pentagonal and hexagonal windows of ~5 Å and ~8.6 Å, respectively [45]. Considering the results of the DFT theoretical study [47] that reported the largest dimension of the sulfur ring (S_8) as ca. 6.88 Å, MIL-100(Fe) can be considered a suitable host for both S_8 and polysulfides, since its structural features are compatible with the insertion of sulfur species, at least into the bigger mesoporous cavities, as depicted in Fig. 1. Molecular graphic representations and analysis were conducted using ToposPro 5.5.2.0 [48] and MERCURY 2.3 [49] software programs.

The excellent correlation between the experimental XRD pattern of the synthesized solid and the simulated pattern for the MIL-100(Fe)
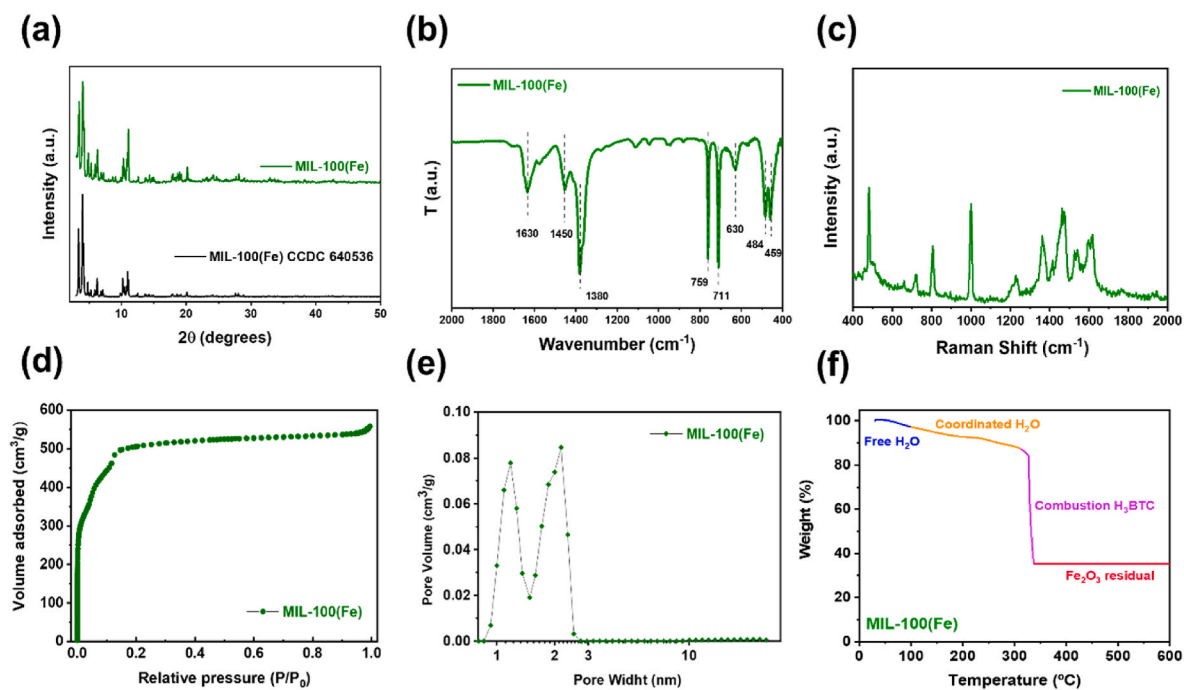
Fig. 2. (a) XRD, (b) FTIR, (c) Raman, (d) N_2 adsorption/desorption isotherms, (e) Pore size distribution and (f) TGA under O_2 flow of MIL-100(Fe).
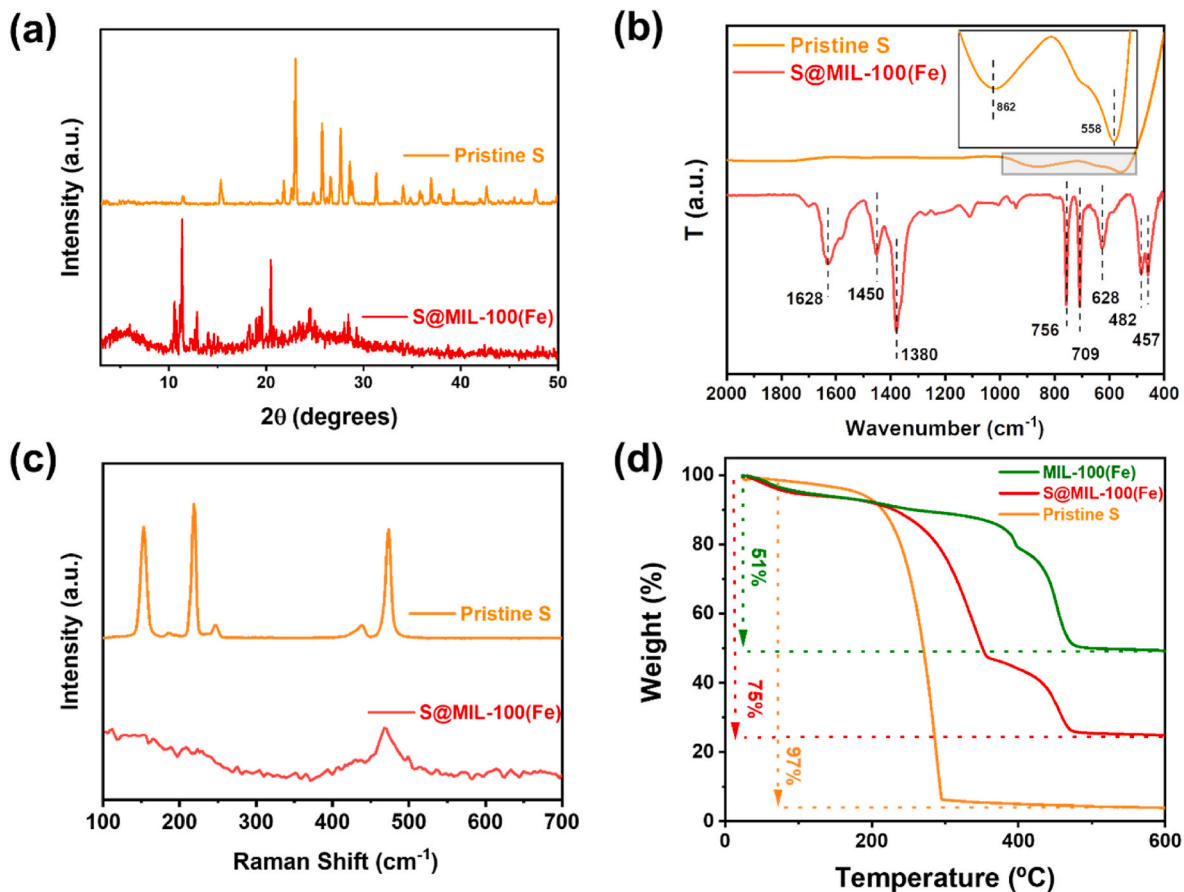

Fig. 3. (a) XRD, (b) FTIR, (c) Raman, and (d) TGA under N_2 flow of S@MIL-100(Fe) and pristine S.

MOF [39] confirmed the obtaining of the desired structure with high crystallinity and purity (Fig. 2a). The XRD pattern of the solid showed no shifts in reflection positions nor the emergence of new peaks with respect to the pre-activated solid, confirming the robustness of MIL-100 (Fe) structure [39] during thermal treatment (Fig. S1). The FTIR spectrum of the synthesized solid, presented in Fig. 2b, shows the
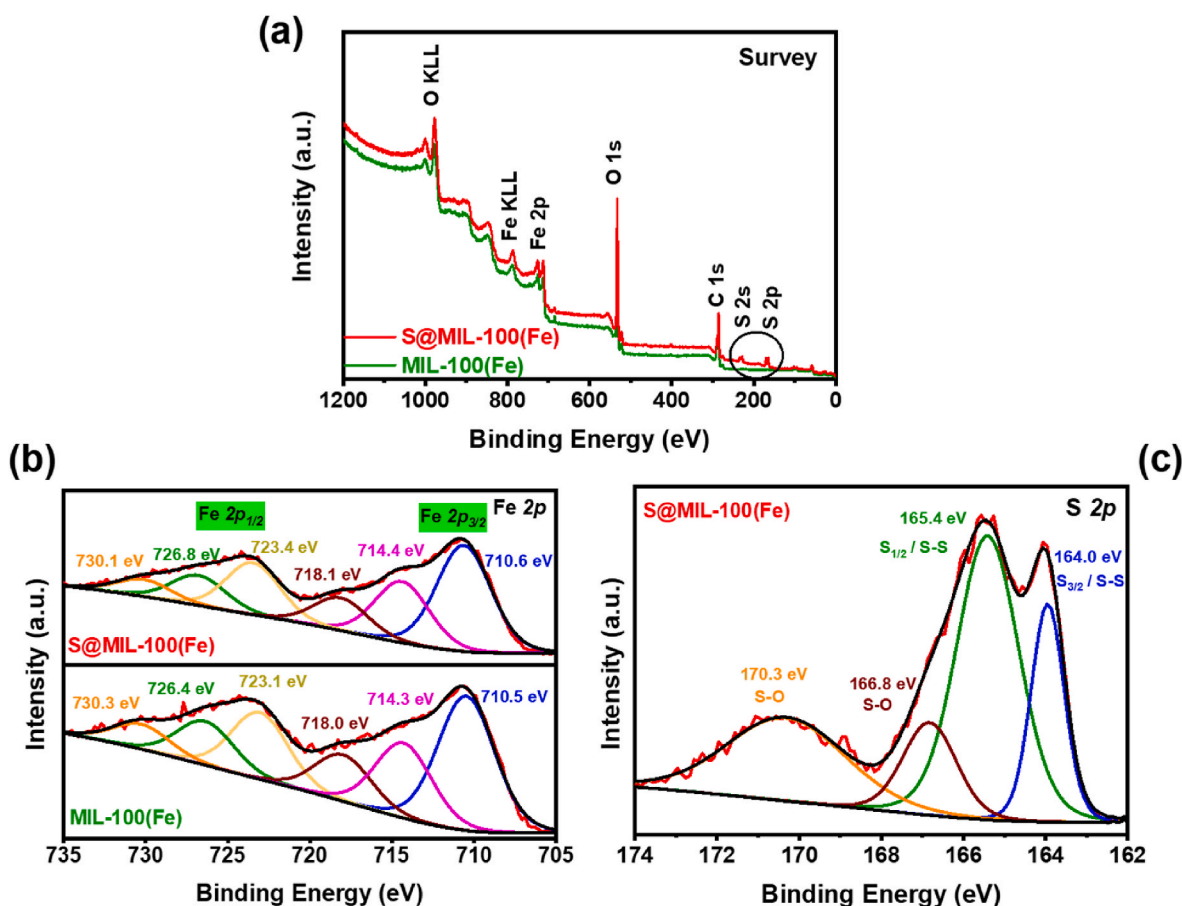
Fig. 4. XPS spectra of MIL-100(Fe) and S@MIL-100(Fe) for (a) survey, (b) Fe*2p*, and (c) S*2p*.

characteristic vibrational modes of the MIL-100(Fe) structure: (1) bands attributed to the carboxylate groups of the 1,3,5-benzenetricarboxylate anions [50,51], with ν_{as}C-O at 1630 cm^{-1}, ν_sC-O at 1450 cm^{-1}, and ν_sC-O at 1380 cm^{-1}; (2) sharp bands at 759 and 711 cm^{-1} corresponding to the C–H bending vibrations of benzene [52,53]; and (3) a signal under 650 cm^{-1} assigned to the ν_{as} (Fe$_3$O) mode [54,55] of the oxo-centered iron(III) PBUs. The Raman spectrum of MIL-100(Fe) in Fig. 2c is identical to that previously reported in the literature [52], which also confirms the correct synthesis of MIL-100(Fe) as evidenced by the XRD characterization. The N$_2$ adsorption-desorption isotherm of MIL-100 (Fe), Fig. 2d, exhibited a mixed I/IV type [52,56], without an evident hysteresis loop [52], very similar to those reported in different studies for materials with the MIL-100(Fe) structure [57–59]. The specific surface area and total pore volume values were within the range reported for the MOF MIL-100(Fe) [41]: 1961 m^2/g and 0.836 cm^3/g, respectively. The pore size distribution, calculated by the DFT method and presented in Fig. 2e, shows that more than 90 % of these values originates from micropores, indicating that this material is predominantly microporous in nature. Hence, these results suggest that the synthesized MIL-100(Fe) has adequate textural properties to potentially serve as a sulfur-host material, consistent with the structural features illustrated in Fig. 1. The TGA plot of MIL-100(Fe) in Fig. 2f shows three stages of weight loss occurring between 30 and 600 °C under O$_2$ flow: (i) initial weight loss (~3 %) up to 100 °C attributed to free H$_2$O, (ii) subsequent weight loss (~10 %) between 100 and 310 °C associated with H$_2$O co-ordinated to the iron-based trimmers, and (iii) final weight loss (~50 %) related to the combustion of H$_3$BTC, giving residual Fe$_2$O$_3$ [60].

3.2. Characterization of S@MIL-100(Fe) composite

The XRD pattern of the S@MIL-100(Fe) composite (Fig. 3a) does not show the characteristic peaks of the orthorhombic structure typical of pristine sulfur, which is the structure in which sulfur crystallizes by the melt diffusion method [61–64]. This discrepancy may arise from sulfur completely infiltrating the pores of the material, with no sulfur present on the surface of the material [64–66]. This behavior has already been previously reported for S@MIL-100(V) [13] and S@MIL-100(Cr) [23] composites prepared via the melt diffusion method. The decrease in intensity or disappearance of low-angle reflections in MIL-100(Fe) XRD patterns has been observed in nanocrystalline MIL-100(Fe) materials [67], as well as in several MIL-100(Fe)-based composites [68–70]. The S@MIL-100(Fe) composite was also analyzed by FTIR (Fig. 3b). After sulfur impregnation, the vibrational modes of MIL-100(Fe) continue to be observed (Fig. 3b); these bands maintain their intensity, indicating the absence of sulfur on the surface of MIL-100(Fe) [71]. Furthermore, the characteristic bands of pristine sulfur do not appear in the S@MIL-100(Fe) composite, further confirming the absence of sulfur on the surface [64]. This finding aligns with previous XRD results. Additionally, the bands corresponding to sulfur are absent in the Raman spectrum of S@MIL-100(Fe) (Fig. 3c). This absence is consistent with the inference drawn from XRD and FTIR analyses that sulfur has fully infiltrated into the pores of the MOF [72]. Using TGA measurements in an inert N$_2$ atmosphere, the sulfur content in the S@MIL-100(Fe) composite was evaluated (Fig. 3d). Thermal treatment in N$_2$ of MIL-100(Fe) and the composite S@MIL-100(Fe) produce a loss of 51 % and 75 %, respectively. By performing mathematical calculations using equation (1), it was determined that the composite is composed of 51 % S and 49 % MIL-100(Fe) by weight. Sulfur is lost at a higher temperature
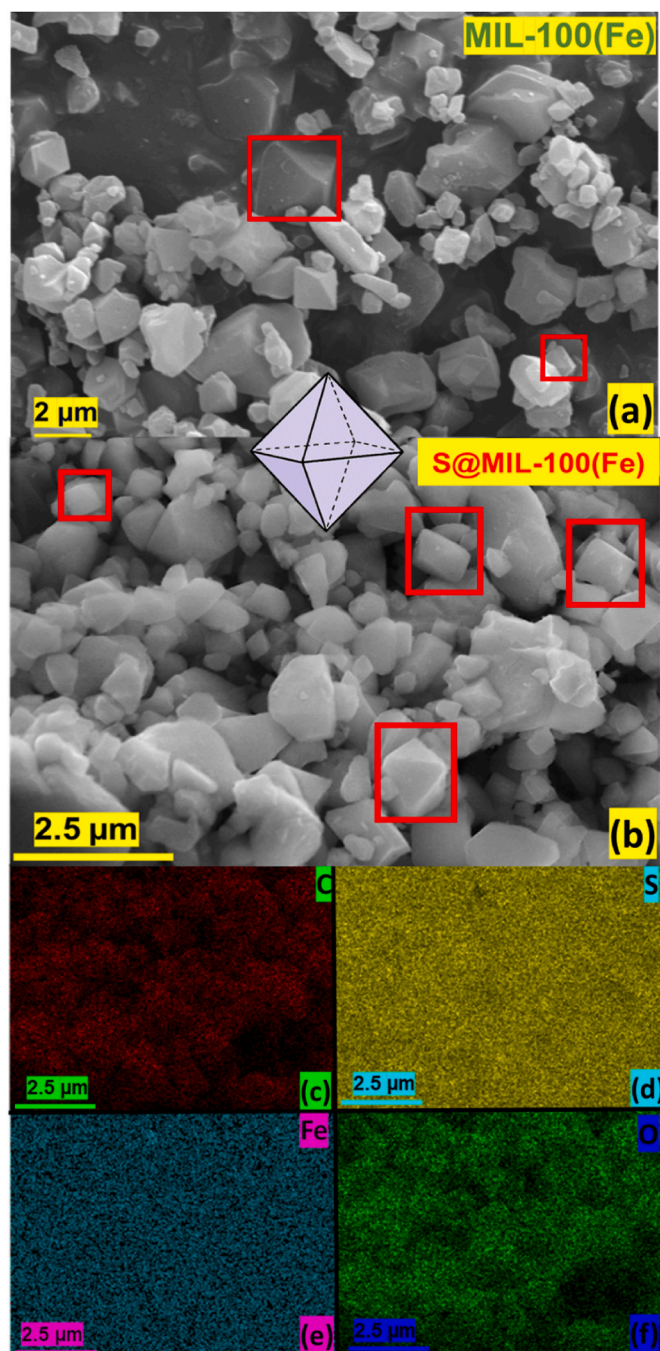
Fig. 5. SEM images of (a) MIL-100(Fe) and (b) S@MIL-100(Fe), along with elemental mapping of C (red), S (yellow), Fe (blue), and O (green) in the S@MIL-100(Fe) composite. (For interpretation of the references to color in this figure legend, the reader is referred to the Web version of this article.)

compared to pristine sulfur because, as previously elucidated, it is located inside the pores of the MOF [42].

$$x \, a + (1-x) \, b = c \tag{1}$$

Where x is the sulfur content in S@MIL-100(Fe), then the content of MIL-100(Fe) is 1-x. While, a, b and c are the weight loss of pristine sulfur, MIL-100(Fe) and S@MIL-100(Fe), respectively. The theoretical sulfur content that can be incorporated within the porosity of the material is related to its pore volume, as per equation (2). A theoretical sulfur loading of 63 % by weight (Ws(%)) is calculated for a total pore volume of 0.836 cm^3/g, slightly exceeding the experimental value of 51

%. This discrepancy confirms that all the sulfur is indeed found within the pores of the material, thereby validating the deductions drawn from XRD, Raman and FTIR analyses [73].

$$W_S \, (\%) \, V = \left[\frac{\rho s \, V}{\rho s \, V + 1} \right] x \, 100 \tag{2}$$

where ρs is the theoretical density of sulfur (2.07 g/cm^3) and V is the pore volume of the matrix.

The XPS spectra of MIL-100(Fe) and S@MIL-100(Fe) are shown in Fig. 4. As observed in Fig. 4a, the spectrum of S@MIL-100(Fe) presents a distinct single signal not observed in the pristine material, MIL-100(Fe), specifically, the signal of S (2s and 2p). The Fe2p spectrum (Fig. 4b), as well as the C1s and O1s spectra (Fig. S2), reveal chemical environments consistent with those reported in the literature for MIL-100(Fe) [52,60]. The Fe $2p_{1/2}$ and the Fe $2p_{3/2}$ was centered at 724.2 and 710.8 eV, respectively. The fitted peaks located at 710.6, 714.4, 723.4 and 726.8 are attributed to Fe(III). Peaks at 718.1 and 730.1 eV represent the shake-up satellites of Fe(III) [60,74]. The C1s spectrum was deconvoluted into three peaks: peaks at 284.6 and 288.5 eV, corresponding to electron binding energies in the phenyl and carboxyl groups, respectively, and the peak at 286.1 eV corresponding to carbon on the surface [75]. Furthermore, as can be seen, the environment of each of the elements is maintained for the S@MIL-100(Fe) composite, indicating that the synthesis of the compound via melt diffusion does not modify the chemical environment of the pristine MOF. The S2p spectrum, Fig. 4c, shows four components associated with two chemical environments: one corresponding to S–S bonds and the other to S–O bonds, situated around 164–166 eV and 167–170 eV, respectively [76].

The nitrogen adsorption-desorption measurements of the composite material are shown in Fig. S3. The composite isotherm is type II according to IUPAC, indicating characteristics typical of non-porous solids. The surface area and total pore volume values of S@MIL-100(Fe) composite decrease with respect to the pristine MIL-100(Fe), confirming the successful infiltration of sulfur into the MIL-100(Fe) porosity, as previously deduced by Raman and XRD analyses. Upon observing the pore size distribution in the inset of Fig. S3, it become evident that sulfur has been incorporated into the microporosity of MIL-100(Fe). The synthesized MIL-100(Fe) and S@MIL-100(Fe) composite both were examined by scanning electron microscopy (SEM), revealing crystals with a broad size distribution. While the morphology of the MOF appeared somewhat irregular, some crystals exhibited the typical octahedral morphology characteristic of MIL-100(Fe) (dimensions = ~5 × 2 μm) (Fig. 5a) [52]. In Fig. 5b, it is evident that the octahedral morphology is maintained in the S@MIL-100(Fe) composite, indicating that the synthesis via melt diffusion did not alter the morphology of the pristine MIL-100(Fe) [38]. Elemental mapping of the S@MIL-100(Fe) composite (Fig. 5c–f) showed uniform distribution of the elements S, C, Fe and O. This result indicates successful and homogeneous impregnation of the MOF with sulfur.

3.3. Electrochemical properties of S@MIL-100(Fe) composite

3.3.1. Li–S batteries

The electrochemical properties of the S@MIL-100(Fe) were characterized by electrochemical impedance spectroscopy (EIS), cyclic voltammetry (CV), and galvanostatic discharge/charge measurements. CV curves were recorded at different scan rates. The curve obtained at a rate of 0.4 mV/s presented in Fig. 6a shows the typical profile for the electrochemical reaction between S and Li, featuring two reduction peaks at 2.38 and 2.00 V, corresponding to the formation of long-chain (S$_8$/Li$_2$S$_X$; $4 \leq x \leq 8$) and short-chain (Li$_2$S$_X$/Li$_2$S$_2$) polysulfides, respectively [77]. Curves recorded at different rates are shown in Fig. S4, and these were employed to calculate the diffusion coefficient of Li$^+$ ions, D$_{Li+}$, using the Randles-Secvik equation (equation (3)).
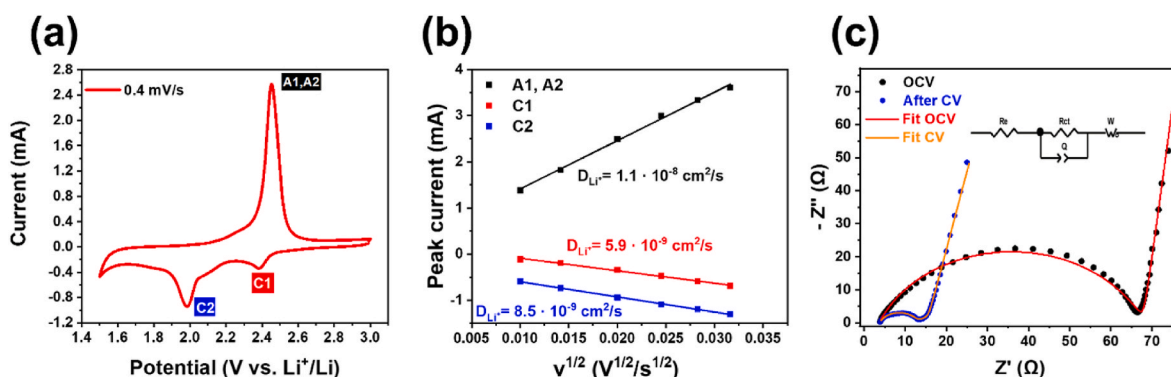
Fig. 6. (a) CV measurements performed between 1.5 and 3 V vs. Li$^+$/Li recorded at 0.4 mV/s, (b) representation of linear fits of peak current intensity (I$_{peak}$) vs. the square root of the scan rate (v$^{1/2}$) necessary for the calculation of Randles-Secvik, (c) EIS curves with fitting before and after recording CV measurements, indexed the equivalent circuit used for the curve fitting.

$$I_{peak} = 0.4463 \left(\frac{n^3 F^3}{RT}\right) AC(D\nu)^{1/2} \qquad (3)$$

where I_{peak} is the peak current intensity, n is the number of electrons involved in the electrochemical reaction, F is Faraday's constant (96,485 C/mol), R is the gas constant (8.314 J/K·mol), T is the temperature (298.15 K), A is the electrode area (1.327 cm^2), C is the concentration of Li$^+$ ions in the electrode (mol/cm^3), and D is the diffusion coefficient (cm^2/s).

We have not found reported D_{Li+} calculations for pristine MOFs or MOF composites. Instead, calculations have only been found for a derivative of the MOF, which reports diffusion values similar to those of the present work (Fig. 6b) [77]. EIS measurements show that the S@MIL-100(Fe) composite exhibits superior transport properties compared to other MIL-100s, such as MIL-100(V) or Mn-MIL-100 [13, 38]. This Nyquist plot can be represented by the equivalent circuit indexed in Fig. 6c. In the high-frequency zone, the electrolytic resistance (Re) can be observed. In the medium-high frequency zone, a defined semicircle is observed, which correspond to the charge transfer process and the formation of the solid electrolyte interphase (SEI) on the surface of the electrode (RctQ). In the low-frequency zone, a semi-infinite inclined line is observed, associated with a Warburg element (W) [78,79]. As can be seen, the main change occurs in the value of Rct before and after the CV; this decrease is due to the increase in electronic and ionic transfer at the electrolyte/cathode interface during cycling, leading to microstructural changes in the cathode [80]. The resistance values are shown in Table S1.

Galvanostatic measurements of the S@MIL-100(Fe) composite were carried out between 0.1C and 2C within a voltage window of 1.7–2.8 V. The discharge curve profile in Fig. 7a shows the two typical plateaus characteristics of the LSBs: the first, located at 2.4 V, corresponding to the solid-liquid reaction involving the opening of the S$_8$ ring and the formation of long-chain LPSs (Li$_2$Sx, $4 \leq x \leq 8$), while the second, at 2 V, is associated with the liquid-solid reaction leading to the formation short-chain LPSs (Li$_2$S$_2$ and Li$_2$S), as shown in the CV curves [81]. From these curves, the polarization was calculated by considering the average voltage of each of the charge and discharge curves. To obtain this average voltage, the area under the curve (dV/dq) was calculated for both charging and discharging, over the maximum capacity (qmax). The hysteresis values increase with the current rate of 0.18 and 0.37 V (Fig. 7b); these values are lower than those of other carbonaceous materials [42,82]. The galvanostatic cycling of the S@MIL-100(Fe) electrode at currents increasing from 0.1C to 2C in order to evaluate the rate capability of the electrode is shown in Fig. 7c. Predictably, the capacity decreases as the current density increases, dropping from 450 mA h/g at 0.1C to 300 mA h/g at 2C. Notably, the electrode demonstrates great stability, with minimal capacity loss despite increased current. Upon

returning to 0.1C, the capacity fully recovers, which shows the great response of the material when subjected to stress.

To study the electrochemical stability of the S@MIL-100(Fe) composite, prolonged galvanostatic cycling was carried out at two different rates: 0.5C and 2C. At a moderate rate of 0.5C, three different performance zones can be distinguished, as shown in Fig. 7d: (i) from cycle 1 to 375, labeled as "Zone I", where the main degradation of the electrode occurs and the decay rate values are at 0.12 %; (ii) from cycle 375 to 1000, labeled as "Zone II", exhibiting greater stability with the decay rate decreasing to 0.045 %; and finally, (iii) until cycle 3000, labeled as "Zone III", where the electrode shows an ultra-stable behavior, reducing the decay rate to values of 0.021 %. With respect to the coulombic efficiency, the ratio between the discharge and charge capacity remains close to 100 % throughout the cycling, indicating low diffusion of LPSs. However, when increasing the rate to a high 2C, a decrease in capacity is observed (Fig. 7e), consistent with findings of the rate capability test. In this case, two performance zones emerge: (i) the initial zone, lasting until cycle 750, labeled as "Zone I", where the main degradation of the electrode occurs, with a loss rate of 0.041 %, as observed from the 0.5C test, and (ii) the subsequent zone, extending until cycle 3000, labeled as "Zone II", characterized by an ultra-stable behavior with a very low loss rate of 0.016. The coulombic efficiency also remains close to 100 %. As illustrated in Fig. S5, neither the metal-organic structure nor the metal center contributes electrochemically in LSBs. The excellent performance can be attributed to the synergistic effects of the highly microporous structure of MIL-100(Fe), which provides an ideal matrix for confining polysulfides, and the strong interactions between Lewis acidic Fe(III) center and the polysulfide base [83]. These interactions significantly slow down the migration of soluble polysulfides out of the pores, leading to the excellent cycling performance of S@MIL-100(Fe) composite.

If we compare these data with the MIL-100 MOF used as cathode matrices in LSBs (Table S2), it's evident that the results are significantly improved. The number of cycles reached in the literature does not exceed 300 cycles, compared to the 3000 achieved in the present study. This greater stability is also reflected in the values of the decay rate per cycle, obtaining lower values with respect to what was observed among other similar materials. Electrochemical tests conducted on other materials based on the MIL-100 MOF have typically been performed at low current densities of 0.1C, in contrast to the present study, which has reached moderate to high rates of 0.5C and 2C.

This stability is due to the great capability of the material to trap LPSs generated during the cycle. To analyze this property, an adsorption measurement of polysulfides, specifically Li$_2$S$_6$, was carried out in the glove box. Fig. S6 shows the images of the pristine Li$_2$S$_6$ solution and the mixed solution of the same polysulfide with the MIL-100(Fe) MOF at two time points: at 0 h (t = 0 h) and at 2 h (t = 2 h). As can be seen, after 2 h, the solution undergoes discoloration upon mixing, while the pristine
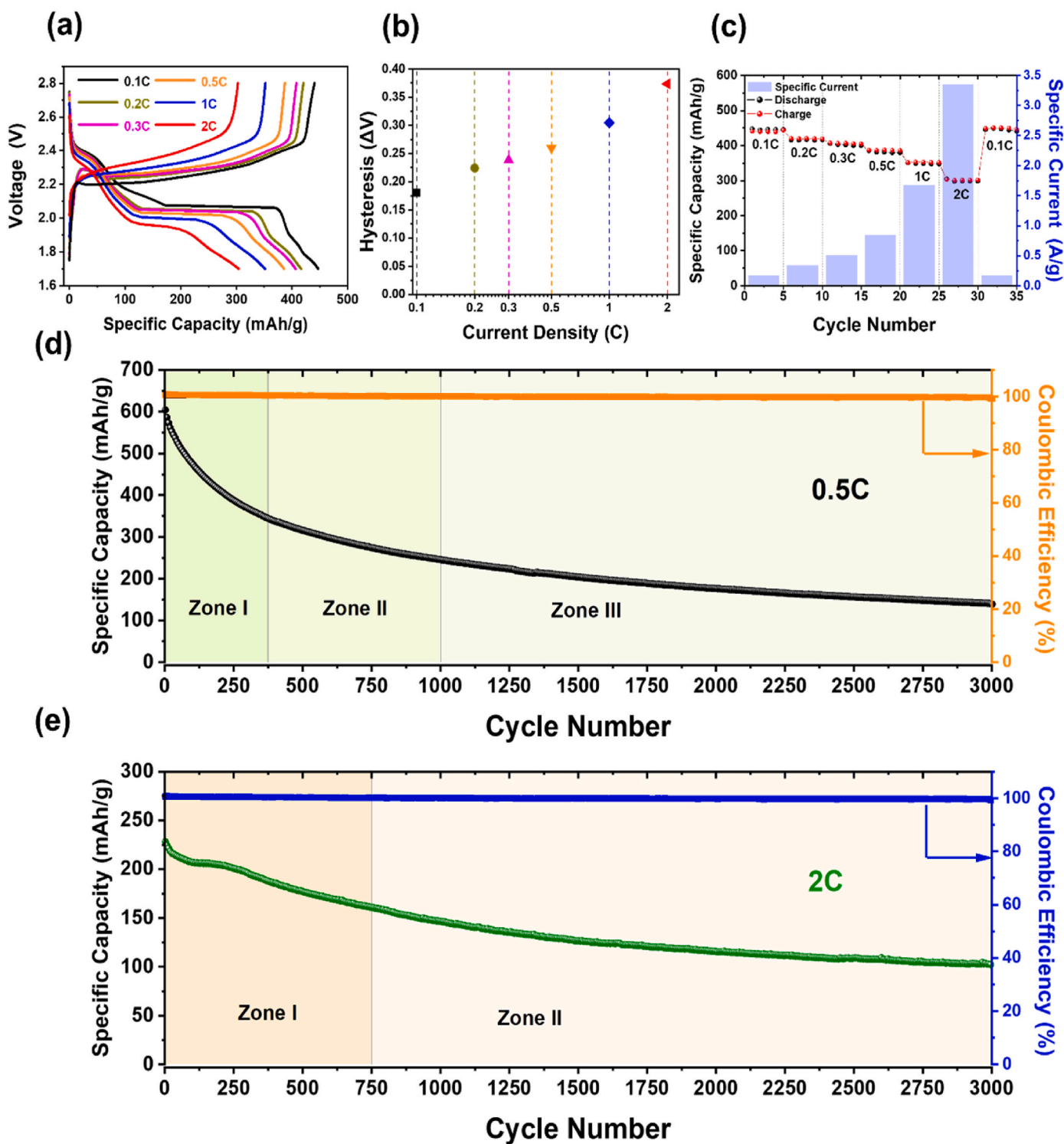
Fig. 7. (a) Galvanostatic charge/discharge curves, (b) polarization voltages calculated from the charge/discharge profiles, (c) rate capability at different current rates (sulfur loading of 1.3 mg/cm^2), (d) and (e) long-term discharge capacity values of S@MIL-100(Fe) as a function of the cycle number at current rates 0.5C and 2C with a sulfur loading of 1.1 mg/cm^2 and 1.5 mg/cm^2, respectively.

solution maintains its original yellow color, characteristic of the long-chain polysulfide. To certify that this discoloration is due to the adsorption of said polysulfide, the UV–Vis spectra of both the pristine solution and the mixed solution was recorded after 2 h, as shown in Fig. S6. From this figure, it evident that the adsorption band at 420 nm corresponding to Li_2S_6 disappears. These results confirm the good adsorption properties of MIL-100(Fe), which are attributed to two

factors: (i) physical confinement associated with its high specific surface area, large volume of micropores, and well-defined structure, and (ii) chemical interaction of the Lewis acid center Fe(III) with the polysulfides [83]. The integration of findings from FTIR, XPS, XRD, and Raman analyses conducted on both MIL-100(Fe) and S@MIL-100(Fe), combined with insights from the Li_2S_6 adsorption test, enable us to suggest the pivotal role of Fe(III)-CUS centers in trapping polysulfides,
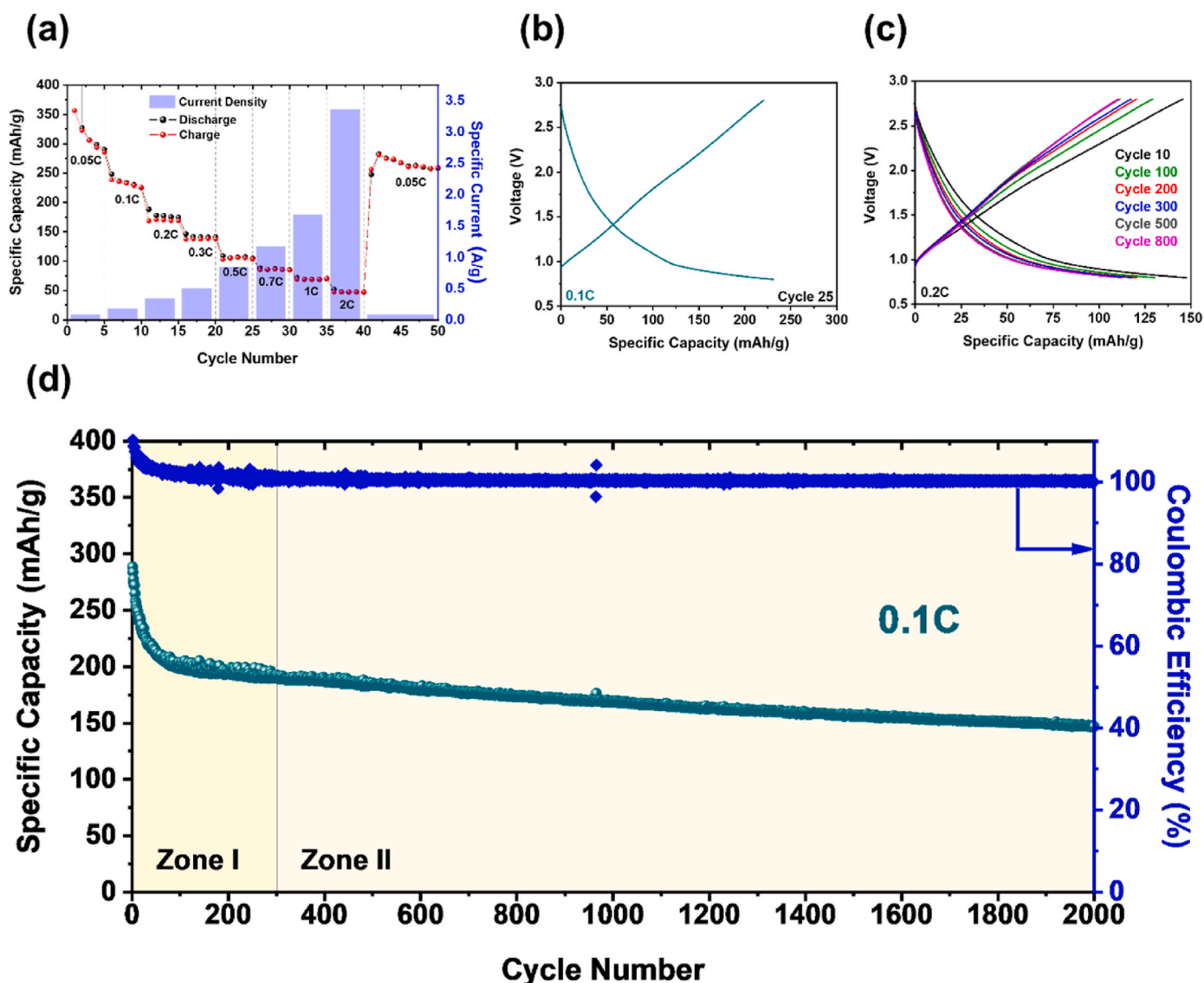
Fig. 8. (a) Rate capability at different current rates, (b) galvanostatic charge/discharge curves in cycle 25 at 0.1C rate, (c) galvanostatic charge/discharge curves in different cycles at 0.2C rate, and (e) long-term discharge capacity values as a function of the cycle number at current rate of 0.1C for S@MIL-100(Fe) with a sulfur loading of 0.8 mg/cm^2.

as depicted in the scheme from Fig. S8.

In the literature, it is not common to find images depicting the morphology of the cathode material based on MOF matrices. As a novelty, this article demonstrates that such morphology is maintained even after the cathode mixture is prepared, as illustrated in Fig. S7a. Additionally, the SEM image of the electrode cycled at a rate of 0.5C, as shown in Fig. S7b, reveals that despite undergoing 3000 cycles, the electrode exhibits minimal cracking, thus preventing the formation of dead zones of active material.

3.3.2. RT Na–S batteries

To demonstrate the material's ability to be a sulfur cathodic matrix, the behavior of MIL-100(Fe) in sodium-sulfur batteries has also been studied. The electrochemical study involved galvanostatic measurements of the S@MIL-100(Fe) composite at rates between 0.05C and 2C within a voltage window of 0.8–2.8 V. To study the performance of the S@MIL-100(Fe) electrode at different current densities, the so-called rate capability was conducted, exposing the electrode to rates ranging from 0.05C to 2C (Fig. 8a). The specific capacity decreases from 300 mA h/g at 0.05C to 50 mA h/g at 2C. Upon returning to a current of 0.05C,

the capacity of the electrode returns to the initial values, which demonstrates its good response to stress. As previously demonstrated, all the sulfur is housed within the pores of the MIL-100(Fe) MOF, preventing direct contact between the sulfur and the solvent. Consequently, the reactions that take place involve conversion reactions within a quasi-solid state, eliminating the formation of long-chain sodium polysulfides, with the formation of reaction intermediates taking place in a solid state. This accounts for the typical profiles observed in quasi-solid-state reactions, as depicted in Fig. 8b [84,85]. This reaction mechanism is based on the hindrance posed by solvent molecules in accessing the microporosity of the material. Consequently, the polysulfide byproducts cannot dissolve and exit these micropores. Thus, this porous environment facilitates the reaction to occur in a quasi-solid state [26] (see Table 1).

The electrochemical stability of the electrode in RT Na–S batteries was studied at two different rates, 0.1C and 0.2C. At 0.1C rate, two performance zones can be distinguished, similar to what occurred in Li–S batteries (Fig. 8d): a first zone extending until cycle 300, "Zone I", with a loss of capacity per cycle of 0.113 %, and a second zone extending until cycle 2000, "Zone II", where stabilization is much greater, with a

Table 1

Capacity retention (mAh/g) and decay rate per cycle (mAh/g and %) calculated in the different zones for 0.5C and 2C rate in LSBs.

Region	Initial capacity (mAh/g)	Capacity retention (mAh/g)	Decay rate per cycle	
			(mAh/g)	(%)
0.5C rate				
Global	621	139	0.161	0.026
Zone I	621	344	0.738	0.119
Zone II	344	246	0.157	0.045
Zone III	245	139	0.053	0.021
2C rate				
Global	233	102	0.044	0.019
Zone I	233	161	0.096	0.041
Zone II	161	102	0.026	0.016

Table 2

Capacity retention (mAh/g) and decay rate per cycle (mAh/g and %) calculated in the different zones at 0.1C in RT Na–S batteries.

Region	Initial capacity (mAh/g)	Capacity retention (mAh/g)	Decay rate per cycle	
			(mAh/g)	(%)
0.1C rate				
Global	288	147	0.071	0.024
Zone I	288	190	0.327	0.113
Zone II	190	147	0.025	0.013

loss per cycle of only 0.013 %. Detailed cyclic stability data are shown in Table 2. Doubling the rate to 0.2C, as shown in Fig. 8c, demonstrates the maintenance of this high stability, with the capacity decreasing only by 6 mA h/g from cycle 300 to cycle 800. Regarding the coulombic efficiency, as expected due to the absence of long chain polysulfides, it remains close to 100 % throughout the cycling at both current densities.

4. Conclusions

This study aimed to assess the MIL-100(Fe) MOF as an unprecedented sulfur cathodic host for both Li–S and Na–S batteries. A composite material based on sulfur hosted in MIL-100(Fe) was obtained. As a new finding, this paper illustrates that the morphology typical of the pristine MOF remains unchanged even after the preparation of the cathode mixture. This composite exhibited a remarkable capacity retention throughout an ultra-long cycling when utilized as a cathode of both Li–S and RT Na–S batteries. Specifically, after 3000 cycles at 2C in Li–S cells, the capacity decreased by only 0.044 mA h per cycle. Similarly, when examining RT Na–S cells, the capacity remained stable with a loss of less than 0.08 % over 2000 cycles at 0.01C-rate. This stability can be attributed to the great and regular porosity of the MIL-100(Fe) structure along with the active sites that have affinity with soluble polysulfides. Thus, the excellent textural properties of the MIL-100(Fe) host, characterized by its high surface area, enables trapping of intermediate polysulfides. Moreover, active centers, especially Fe^{III} CUS, generated through thermal activation under vacuum, act as Lewis acidic sites with strong affinity for soluble polysulfides of basic nature. Overall, the use of MIL-100(Fe) as sulfur-host inhibits the migration of polysulfides to the electrolyte and thus the *shuttle effect* and loss of active material. Comparing MIL-100 MOFs utilized in Li–S batteries in the literature, our work represents a significant advancement. Previously, MIL-100 materials have been tested for fewer cycles, typically not exceeding 300 cycles. In contrast, our MIL-100(Fe) has been tested for 3000 cycles, demonstrating notable stability throughout the entire cycling process. The SEM image of the electrode cycled at 0.5C for 3000

cycles shows minimal cracking, preventing the formation of inactive zones. Furthermore, previous studies on MIL-100 materials have typically utilized low current densities, maxing out at 0.1 C. In our study, MIL-100(Fe) was tested at moderate to high rates of 0.5 and 2C. EIS measurements revealed that the S@MIL-100(Fe) composite exhibits superior transport properties compared to other MIL-100 variants explored in previous studies. In addition, adsorption experiments combined with UV–visible analysis demonstrated the MIL-100(Fe)'s efficacy in anchoring Li_2S_6. Also, the composite electrode showed structural stability on prolonged cycling. Additionally, our research marks the first utilization of a MIL-100 material in the RT Na–S system, also demonstrating high stability at both 0.1C and 0.2C rates. Overall, these findings underscore the potential of MIL-100(Fe) as a promising cathodic host for Metal-Sulfur batteries, offering superior capacity retention, which is crucial for enhancing battery performance and longevity. Future research should aim to corroborate the precise mechanisms involved during the galvanostatic charge and discharge of sodium-sulfur cells.

CRediT authorship contribution statement

Álvaro Bonilla: Writing – original draft, Investigation, Data curation. **Gabriela A. Ortega-Moreno:** Writing – original draft, Investigation, Formal analysis. **María C. Bernini:** Writing – review & editing, Validation, Supervision, Resources, Methodology, Investigation. **Juan Luis Gómez-Cámer:** Writing – original draft, Validation, Supervision. **Lucía Isabel Barbosa:** Writing – review & editing, Writing – original draft, Visualization, Supervision, Methodology, Conceptualization. **Álvaro Caballero:** Writing – review & editing, Visualization, Supervision, Resources, Methodology, Funding acquisition, Conceptualization.

Declaration of competing interest

The authors declare the following financial interests/personal relationships which may be considered as potential competing interests: Alvaro Caballero reports financial support was provided by Spain Ministry of Science and Innovation. If there are other authors, they declare that they have no known competing financial interests or personal relationships that could have appeared to influence the work reported in this paper.

Data availability

Data will be made available on request.

Acknowledgments

Appendix A. Supplementary data

Supplementary data to this article can be found online at https://doi.org/10.1016/j.jpowsour.2024.234613.

References

[1] M. Groll, Can climate change be avoided? Vision of a hydrogen-electricity energy economy, Energy 264 (2023) 126029, https://doi.org/10.1016/j.energy.2022.126029.

[2] T. Mageto, S.D. Bhoyate, F.M. de Souza, K. Mensah-Darkwa, A. Kumar, R.K. Gupta, Developing practical solid-state rechargeable Li-ion batteries: concepts, challenges, and improvement strategies, J. Energy Storage 55 (2022) 105688, https://doi.org/10.1016/j.est.2022.105688.

[3] D. Pahari Nagmani, P. Verma, S. Puravankara, Are Na-ion batteries nearing the energy storage tipping point? – Current status of non-aqueous, aqueous, and solid-sate Na-ion battery technologies for sustainable energy storage, J. Energy Storage 56 (2022) 105961, https://doi.org/10.1016/j.est.2022.105961.

[4] W. Wang, B. Yuan, Q. Sun, R. Wennersten, Application of energy storage in integrated energy systems — a solution to fluctuation and uncertainty of renewable energy, J. Energy Storage 52 (2022) 104812, https://doi.org/10.1016/j.est.2022.104812.

[5] D.K. Kim, K.H. Rho, Y. Na, M. Kim, Evaluation of energy storage technologies for efficient usage of wind power in the far-eastern region: a techno-economic analysis, J. Energy Storage 39 (2021) 102595, https://doi.org/10.1016/j.est.2021.102595.

[6] J. Cho, S. Jeong, Y. Kim, Commercial and research battery technologies for electrical energy storage applications, Prog. Energy Combust. Sci. 48 (2015) 84–101, https://doi.org/10.1016/j.pecs.2015.01.002.

[7] Q. Zheng, N. Deng, Y. Zhao, L. Gao, B. Cheng, W. Kang, A review on 1D materials for all-solid-state lithium-ion batteries and all-solid-state lithium-sulfur batteries, Chem. Eng. J. 451 (2023) 138532, https://doi.org/10.1016/j.cej.2022.138532.

[8] N. Deng, Y. Li, Q. Li, Q. Zeng, S. Luo, H. Wang, W. Kang, B. Cheng, Multi-functional yolk-shell structured materials and their applications for high-performance lithium ion battery and lithium sulfur battery, Energy Storage Mater. 53 (2022) 684–743, https://doi.org/10.1016/j.ensm.2022.08.003.

[9] J. Zhou, R. Li, X. Fan, Y. Chen, R. Han, W. Li, J. Zheng, B. Wang, X. Li, Rational design of a metal–organic framework host for sulfur storage in fast, long-cycle Li–S batteries, Energy Environ. Sci. 7 (2014) 2715–2724, https://doi.org/10.1039/C4EE01382D.

[10] S.-E. Cheon, K.-S. Ko, J.-H. Cho, S.-W. Kim, E.-Y. Chin, H.-T. Kim, Rechargeable lithium sulfur battery: rate capability and cycle characteristics, J. Electrochem. Soc. 150 (2003) A800–A805, https://doi.org/10.1149/1.1571533.

[11] A. Benítez, J. Amaro-Gahete, D. Esquivel, F.J. Romero-Salguero, J. Morales, Á. Caballero, MIL-88A metal-organic framework as a stable sulfur-host cathode for long-cycle Li-S batteries, Nanomaterials 10 (2020) 424, https://doi.org/10.3390/nano10030424.

[12] Y. Jeoun, M.-S. Kim, S.-H. Lee, J. Hyun Um, Y.-E. Sung, S.-H. Yu, Lean-electrolyte lithium-sulfur batteries: recent advances in the design of cell components, Chem. Eng. J. 450 (2022) 138209, https://doi.org/10.1016/j.cej.2022.138209.

[13] Y. Hou, H. Mao, L. Xu, MIL-100(V) and MIL-100(V)/rGO with various valence states of vanadium ions as sulfur cathode hosts for lithium-sulfur batteries, Nano Res. 10 (2017) 344–353, https://doi.org/10.1007/s12274-016-1326-0.

[14] Y. He, Z. Chang, S. Wu, H. Zhou, Effective strategies for long-cycle life lithium-sulfur batteries, J. Mater. Chem. A 6 (2018) 6155–6182, https://doi.org/10.1039/c8ta01115j.

[15] V.K. Tomer, R. Malik, J. Tjong, M. Sain, State and future implementation perspectives of porous carbon-based hybridized matrices for lithium sulfur battery, Coord. Chem. Rev. 481 (2023) 215055, https://doi.org/10.1016/j.ccr.2023.215055.

[16] L. Zhou, D.L. Danilov, R.-A. Eichel, P.H.L. Notten, Host materials anchoring polysulfides in Li – S batteries reviewed, Adv. Energy Mater. 11 (2021) 2001304, https://doi.org/10.1002/aenm.202001304.

[17] D. Zhu, T. Long, B. Xu, Y. Zhao, H. Hong, R. Liu, F. Meng, J. Liu, Recent advances in interlayer and separator engineering for lithium-sulfur batteries, J. Energy Chem. 57 (2021) 41–60, https://doi.org/10.1016/j.jechem.2020.08.039.

[18] C. Li, R. Liu, Y. Xiao, F. Cao, H. Zhang, Recent progress of separators in lithium-sulfur batteries, Energy Storage Mater. 40 (2021) 439–460, https://doi.org/10.1016/j.ensm.2021.05.034.

[19] C. Yan, X.-Q. Zhang, J.-Q. Huang, Q. Liu, Q. Zhang, Lithium-anode protection in lithium–sulfur batteries, Trends Chem. 1 (2019) 693–704, https://doi.org/10.1016/j.trechm.2019.06.007.

[20] Y. Liu, Y. Elias, J. Meng, D. Aurbach, R. Zou, D. Xia, Q. Pang, Electrolyte solutions design for lithium-sulfur batteries, Joule 5 (2021) 2323–2364, https://doi.org/10.1016/j.joule.2021.06.009.

[21] X. Liang, L. Wang, X. Wu, X. Feng, Q. Wu, Y. Sun, H. Xiang, J. Wang, Solid-state electrolytes for solid-state lithium-sulfur batteries: comparisons, advances and prospects, J. Energy Chem. 73 (2022) 370–386, https://doi.org/10.1016/j.jechem.2022.06.035.

[22] W. Li, X. Guo, P. Geng, M. Du, Q. Jing, X. Chen, G. Zhang, H. Li, Q. Xu, P. Braunstein, H. Pang, Rational design and general synthesis of multimetallic metal–organic framework nano-octahedra for enhanced Li–S battery, Adv. Mater. 33 (2021) 2105163, https://doi.org/10.1002/adma.202105163.

[23] R. Demir-Cakan, M. Morcrette, F. Nouar, C. Davoisne, T. Devic, D. Gonbeau, R. Dominko, C. Serre, G. Férey, J.M. Tarascon, Cathode composites for Li-S batteries via the use of oxygenated porous architectures, J. Am. Chem. Soc. 133 (2011) 16154–16160, https://doi.org/10.1021/ja2062659.

[24] R. Yan, T. Ma, M. Cheng, X. Tao, Z. Yang, F. Ran, S. Li, B. Yin, C. Cheng, W. Yang, Metal–organic-framework-derived nanostructures as multifaceted electrodes in metal–sulfur batteries, Adv. Mater. 33 (2021) 2008784, https://doi.org/10.1002/adma.202008784.

[25] Z. Huang, P. Jaumaux, B. Sun, X. Guo, D. Zhou, D. Shanmukaraj, M. Armand, T. Rojo, G. Wang, High-energy room-temperature sodium–sulfur and sodium–selenium batteries for sustainable energy storage, Electrochem. Energy Rev. 6 (2023) 21, https://doi.org/10.1007/s41918-023-00182-w.

[26] J. Zhou, S. Xu, Y. Yang, Strategies for polysulfide immobilization in sulfur cathodes for room-temperature sodium–sulfur batteries, Small 17 (2021) 2100057, https://doi.org/10.1002/smll.202100057.

[27] O.M. Yaghi, M.J. Kalmutzki, C.S. Diercks, Metal-Organic Frameworks and Covalent Organic Frameworks, Wiley-VCH, 2019, https://doi.org/10.1002/9783527821099.

[28] S.R. Batten, N.R. Champness, X. Chen, J. Garcia-Martinez, S. Kitagawa, L. Öhrström, M.O. Keeffe, M.P. Suh, J. Reedijk, Terminology of metal–organic frameworks and coordination polymers, Pure Appl. Chem. 85 (2013) 1715–1724, https://doi.org/10.1351/PAC-REC-12-11-20.

[29] A.S. Lawrence, B. Sivakumar, A. Dhakshinamoorthy, Detecting Lewis acid sites in metal-organic frameworks by density functional theory, Mol. Catal. 517 (2022) 112042, https://doi.org/10.1016/j.mcat.2021.112042.

[30] A.-R. Kim, T.-U. Yoon, E.-J. Kim, J.W. Yoon, S.-Y. Kim, J.W. Yoon, Y.K. Hwang, J.-S. Chang, Y.-S. Bae, Facile loading of Cu(I) in MIL-100(Fe) through redox-active Fe (II) sites and remarkable propylene/propane separation performance, Chem. Eng. J. 331 (2018) 777–784, https://doi.org/10.1016/j.cej.2017.09.016.

[31] Z. Li, L. Sun, K. Wang, Y. Zhang, Wide application of metal-organic frameworks in lithium–sulfur battery, Mater. Today Sustain. 22 (2023) 100392, https://doi.org/10.1016/j.mtsust.2023.100392.

[32] J. Zheng, J. Tian, D. Wu, M. Gu, W. Xu, C. Wang, F. Gao, M.H. Engelhard, J.-G. Zhang, J. Liu, J. Xiao, Lewis acid-base interactions between polysulfides and metal organic framework in lithium sulfur batteries, Nano Lett. 14 (2014) 2345–2352, https://doi.org/10.1021/nl404721h.

[33] P. Horcajada, F. Salles, S. Wuttke, T. Devic, D. Heurtaux, G. Maurin, A. Vimont, M. Daturi, O. David, E. Magnier, N. Stock, Y. Filinchuk, D. Popov, C. Riekel, G. Férey, C. Serre, How linker's modification controls swelling properties of highly flexible iron(III) dicarboxylates MIL-88, J. Am. Chem. Soc. 133 (2011) 17839–17847, https://doi.org/10.1021/ja206936e.

[34] S. Surblé, C. Serre, C. Mellot-Draznieks, F. Millange, G. Ferey, A new isoreticular class of metal-organic-frameworks with the MIL-88 topology, Chem. Commun. (2006) 284–286, https://doi.org/10.1039/b512169h.

[35] J.W. Yoon, Y. Seo, Y.K. Hwang, J.-S. Chang, H. Leclerc, S. Wuttke, P. Bazin, A. Vimont, M. Daturi, E. Bloch, P.L. Llewellyn, C. Serre, P. Horcajada, J.-M. Grenehe, A.E. Rodrigues, G. Férey, Controlled reducibility of a metal-organic framework with coordinatively unsaturated sites for preferential gas sorption, Angew. Chem. Int. Ed. 49 (2010) 5949–5952, https://doi.org/10.1002/anie.201001230.

[36] M. Rivera-Torrente, L.D.B. Mandemaker, M. Filez, G. Delen, B. Seoane, F. Meirer, B.M. Weckhuysen, Spectroscopy, microscopy, diffraction and scattering of archetypal MOFs: formation, metal sites in catalysis and thin films, Chem. Soc. Rev. 49 (2020) 6694–6732, https://doi.org/10.1039/d0cs00635a.

[37] J. Tang, J. Wang, Metal organic framework with coordinatively unsaturated sites as efficient fenton-like catalyst for enhanced degradation of sulfamethazine, Environ. Sci. Technol. 52 (2018) 5367–5377, https://doi.org/10.1021/acs.est.8b00092.

[38] W. Li, X. Guo, P. Geng, M. Du, Q. Jing, X. Chen, G. Zhang, H. Li, Q. Xu, P. Braunstein, H. Pang, Rational design and general synthesis of multimetallic metal–organic framework nano-octahedra for enhanced Li–S battery, Adv. Mater. 33 (2021) 2105163, https://doi.org/10.1002/adma.202105163.

[39] P. Horcajada, S. Surble, C. Serre, D.-Y. Hong, Y.-K. Seo, J.-S. Chang, J.-M. Greneche, I. Margiolaki, G. Ferey, Synthesis and catalytic properties of MIL-100 (Fe), an iron(III) carboxylate with large pores, Chem. Commun. (2007) 2820–2822, https://doi.org/10.1039/b704325b.

[40] S. Dou, X. Li, X. Wang, Rational design of metal-organic frameworks towards efficient electrocatalysis, ACS Mater. Lett. 2 (2020) 1251–1267, https://doi.org/10.1021/acsmaterialslett.0c00229.

[41] Y.-K. Seo, J.W. Yoon, J.S. Lee, U.-H. Lee, Y.K. Hwang, C.-H. Jun, P. Horcajada, C. Serre, J.-S. Chang, Large scale fluorine-free synthesis of hierarchically porous iron(III) trimesate MIL-100(Fe) with a zeolite MTN topology, Microporous Mesoporous Mater. 157 (2012) 137–145, https://doi.org/10.1016/j.micromeso.2012.02.027.

[42] Á. Bonilla, A. Benítez, J.L. Gómez-Cámer, Á. Caballero, Impact of composite preparation method on the electrochemical performance of lithium–sulfur batteries, J. Alloys Compd. 968 (2023) 171810, https://doi.org/10.1016/j.jallcom.2023.171810.

[43] S. Brunauer, P.H. Emmett, E. Teller, Adsorption of gases in multimolecular layers, J. Am. Chem. Soc. 60 (1938) 309–319, https://doi.org/10.1021/ja01269a023.

[44] F. Rouquerol, J. Rouquerol, K. Sing, Adsorption by Powders and Porous Solids, Academic Press, 1999.

[45] P. Horcajada, C. Serre, M. Vallet-Regí, M. Sebban, F. Taulelle, G. Férey, Metal-organic frameworks as efficient materials for drug delivery, Angew. Chem. Int. Ed. 45 (2006) 5974–5978, https://doi.org/10.1002/anie.200601878.

[46] Y. Fang, Z. Yang, H. Li, X. Liu, MIL-100(Fe) and its derivatives: from synthesis to application for wastewater decontamination, Environ. Sci. Pollut. Res. 27 (2020) 4703–4724, https://doi.org/10.1007/s11356-019-07318-w.

[47] S. Xin, L. Gu, N.-H. Zhao, Y.-X. Yin, L.-J. Zhou, Y.-G. Guo, L.-J. Wan, Smaller sulfur molecules promise better lithium-sulfur batteries, J. Am. Chem. Soc. 134 (2012) 18510–18513, https://doi.org/10.1021/ja308170k.

[48] V.A. Blatov, A.P. Shevchenko, D.M. Proserpio, Applied topological analysis of crystal structures with the program package ToposPro, Cryst. Growth Des. 14 (2014) 3576–3586, https://doi.org/10.1021/cg500498k.

[49] C.F. Macrae, I.J. Bruno, J.A. Chisholm, P.R. Edgington, P. McCabe, E. Pidcock, L. Rodriguez-Monge, R. Taylor, J. Van De Streek, P.A. Wood, Mercury CSD 2.0 - new features for the visualization and investigation of crystal structures, J. Appl. Crystallogr. 41 (2008) 466–470, https://doi.org/10.1107/S0021889807067908.

[50] K. Nakamoto, Infrared and Raman spectra of inorganic and coordination compounds. Handbook of vibrational spectroscopy, Handb. Vib. Spectrosc. (2006) 1872–1892, https://doi.org/10.1002/9780470027325.s4104.

[51] X. Li, W. Guo, Z. Liu, R. Wang, H. Liu, Fe-based MOFs for efficient adsorption and degradation of acid orange 7 in aqueous solution via persulfate activation, Appl. Surf. Sci. 369 (2016) 130–136, https://doi.org/10.1016/j.apsusc.2016.02.037.

[52] H. Lv, H. Zhao, T. Cao, L. Qian, Y. Wang, G. Zhao, Efficient degradation of high concentration azo-dye wastewater by heterogeneous Fenton process with iron-based metal-organic framework, J. Mol. Catal. Chem. 400 (2015) 81–89, https://doi.org/10.1016/j.molcata.2015.02.007.

[53] N.M. Mahmoodi, J. Abdi, M. Oveisi, M.A. Asli, M. Vossoughi, Metal-organic framework (MIL-100 (Fe)): synthesis, detailed photocatalytic dye degradation ability in colored textile wastewater and recycling, Mater. Res. Bull. 100 (2018) 357–366, https://doi.org/10.1016/j.materresbull.2017.12.033.

[54] H. Leclerc, A. Vimont, J.-C. Lavalley, M. Daturi, A.D. Wiersum, P.L. Llwellyn, P. Horcajada, G. Férey, C. Serre, Infrared study of the influence of reducible iron (III) metal sites on the adsorption of CO, CO2, propane, propene and propyne in the mesoporous metal-organic framework MIL-100, Phys. Chem. Chem. Phys. 13 (2011) 11748–11756, https://doi.org/10.1039/c1cp20502a.

[55] R. Wu, U.A. Jayasooriya, R.D. Cannon, Vibrational coupling in oxo-centred trinuclear clusters: oxygen-16/18 isotopic substitution studies of [Fe3IIIO(O2CC (CH3)3)6(py)3][FeCl4] and [Fe2IIIFeIIO(O2CC(CH3)3)6(py)3], Spectrochim. Acta Part A Mol. Biomol. Spectrosc. 56 (2000) 575–579, https://doi.org/10.1016/S1386-1425(99)00156-0.

[56] Y. Pei, J. Qin, J. Wang, Y. Hu, Fe-based metal organic framework derivative with enhanced Lewis acidity and hierarchical pores for excellent adsorption of oxygenated volatile organic compounds, Sci. Total Environ. 790 (2021) 148132, https://doi.org/10.1016/j.scitotenv.2021.148132.

[57] Y. Devi, I. Ang, F.E. Soetaredjo, S.P. Santoso, W. Irawaty, M. Yuliana, A. E. Angkawijaya, S.B. Hartono, P.L. Tran-Nguyen, S. Ismadji, Y.H. Ju, An iron–carboxylate-based metal–organic framework for Furosemide loading and release, J. Mater. Sci. 55 (2020) 13785–13798, https://doi.org/10.1007/s10853-020-05009-3.

[58] H. Shi, Z. Gu, M. Han, C. Chen, Z. Chen, J. Ding, Q. Wang, H. Wan, G. Guan, Preparation of heterogeneous interfacial catalyst benzimidazole-based acid ILs@ MIL-100(Fe) and its application in esterification, Colloids Surfaces A Physicochem. Eng. Asp. 608 (2021) 125585, https://doi.org/10.1016/j.colsurfa.2020.125585.

[59] N. Yao, Y. Zhang, R. Zhang, L. Zhang, D. Yue, One-step fabrication of HNBR/MIL-100 composites via selective hydrogenation of acrylonitrile-butadiene rubber with a catalyst derived from MIL-100(Fe), J. Mater. Sci. 56 (2021) 326–336, https://doi.org/10.1007/s10853-020-05227-9.

[60] X. Zheng, L. Zhang, Z. Fan, Y. Cao, L. Shen, C. Au, L. Jiang, Enhanced catalytic activity over MIL-100(Fe) with coordinatively unsaturated Fe2+/Fe3+ sites for selective oxidation of H2S to sulfur, Chem. Eng. J. 374 (2019) 793–801, https://doi.org/10.1016/j.cej.2019.05.228.

[61] B.E. Warren, J.T. Burwell, The structure of rhombic sulphur, J. Chem. Phys. 3 (1935) 6–8, https://doi.org/10.1063/1.1749557.

[62] I. Marri, Z. Edfouf, A. Caballero, A.Y. Tesio, Valorisation of argan seeds: production of cathode material for high-performance lithium-sulphur batteries, J. Energy Storage 82 (2024) 110518, https://doi.org/10.1016/j.est.2024.110518.

[63] L. Xia, Z. Song, L. Zhou, D. Lin, Q. Zheng, Nitrogen and oxygen dual-doped hierarchical porous carbon derived from rapeseed meal for high performance lithium–sulfur batteries, J. Solid State Chem. 270 (2019) 500–508, https://doi.org/10.1016/j.jssc.2018.12.031.

[64] M.M.U. Din, B.K. Sahu, A. Das, R. Murugan, Enhanced electrochemical performance of lithium–sulphur battery by negating polysulphide shuttling and interfacial resistance through aluminium nanolayer deposition on a polypropylene separator, Ionics 25 (2019) 1645–1657, https://doi.org/10.1007/s11581-019-02891-z.

[65] F. Sultanov, N. Zhumasheva, A. Dangaliyeva, A. Zhaisanova, N. Baikalov, B. Tatykayev, M. Yeleuov, Z. Bakenov, A. Mentbayeva, Enhancing lithium-sulfur battery performance with biomass-derived graphene-like porous carbon and NiO nanoparticles composites, J. Power Sources 593 (2024) 233959, https://doi.org/10.1016/j.jpowsour.2023.233959.

[66] M. Yu, R. Li, Y. Tong, Y. Li, C. Li, J.D. Hong, G. Shi, A graphene wrapped hair-derived carbon/sulfur composite for lithium-sulfur batteries, J. Mater. Chem. A 3 (2015) 9609–9615, https://doi.org/10.1039/c5ta00651a.

[67] S.D. Taherzade, J. Soleimannejad, A. Tarlani, Application of metal-organic framework nano-MIL-100(Fe) for sustainable release of doxycycline and tetracycline, Nanomaterials 7 (2017) 215, https://doi.org/10.3390/nano7080215.

[68] X. Chen, Y. Zhang, X. Kong, Z. Guo, W. Xu, Z. Fang, S. Wang, L. Liu, Y. Liu, J. Zhang, Controlling crystal growth of MIL-100(Fe) on Ag nanowire surface for optimizing catalytic performance, RSC Adv. 10 (2020) 25260–25265, https://doi.org/10.1039/d0ra04211k.

[69] J. Peng, S. Xian, J. Xiao, Y. Huang, Q. Xia, H. Wang, Z. Li, A supported Cu(I)@MIL-100(Fe) adsorbent with high CO adsorption capacity and CO/N2 selectivity, Chem. Eng. J. 270 (2015) 282–289, https://doi.org/10.1016/j.cej.2015.01.126.

[70] B. Xu, X. Li, Z. Chen, T. Zhang, C. Li, Pd@MIL-100(Fe) composite nanoparticles as efficient catalyst for reduction of 2/3/4-nitrophenol: synergistic effect between Pd and MIL-100(Fe), Microporous Mesoporous Mater. 255 (2018) 1–6, https://doi.org/10.1016/j.micromeso.2017.07.008.

[71] B.H. Park, Y. Jung, S. Kim, Particle size control influence on the electrochemical properties of sulfur deposited on metal organic frameworks host electrodes, J. Inorg. Organomet. Polym. Mater. 31 (2021) 1931–1938, https://doi.org/10.1007/s10904-021-01901-w.

[72] A.Y. Tesio, J.L. Gómez-Cámer, J. Morales, A. Caballero, Simple and sustainable preparation of nonactivated porous carbon from brewing waste for high-performance lithium–sulfur batteries, ChemSusChem 13 (2020) 3439–3446, https://doi.org/10.1002/cssc.202000969.

[73] F. Luna-Lama, A. Caballero, J. Morales, Synergistic effect between PPy:PSS copolymers and biomass-derived activated carbons: a simple strategy for designing sustainable high-performance Li–S batteries, Sustain. Energy Fuels 6 (2022) 1568–1586, https://doi.org/10.1039/D1SE02052H.

[74] N. Geng, W. Chen, H. Xu, M. Ding, T. Lin, Q. Wu, L. Zhang, Insights into the novel application of Fe-MOFs in ultrasound-assisted heterogeneous Fenton system: efficiency, kinetics and mechanism, Ultrason. Sonochem. 72 (2021) 105411, https://doi.org/10.1016/j.ultsonch.2020.105411.

[75] F. Zhang, Y. Jin, J. Shi, Y. Zhong, W. Zhu, M.S. El-Shall, Polyoxometalates confined in the mesoporous cages of metal-organic framework MIL-100(Fe): efficient heterogeneous catalysts for esterification and acetalization reactions, Chem. Eng. J. 269 (2015) 236–244, https://doi.org/10.1016/j.cej.2015.01.092.

[76] S. Wu, J. Wang, S. Song, D.-H. Xia, Z. Zhang, Z. Gao, J. Wang, W. Jin, W. Hu, Factors influencing passivity breakdown on UNS N08800 in neutral chloride and thiosulfate solutions, J. Electrochem. Soc. 164 (2017) C94–C103, https://doi.org/10.1149/2.0541704jes.

[77] F.J. Soler-Piña, J. Morales, Á. Caballero, Synergy between highly dispersed Ni nanocrystals and graphitized carbon derived from a single source as a strategy for high performance Lithium-Sulfur batteries, J. Colloid Interface Sci. 640 (2023) 990–1004, https://doi.org/10.1016/j.jcis.2023.03.035.

[78] T.Q. Nguyen, C. Breitkopf, Determination of diffusion coefficients using impedance spectroscopy data, J. Electrochem. Soc. 165 (2018) E826–E831, https://doi.org/10.1149/2.1151814jes.

[79] A. Benítez, V. Marangon, C. Hernández-Rentero, Á. Caballero, J. Morales, J. Hassoun, Porous Cr2O3@C composite derived from metal organic framework in efficient semi-liquid lithium-sulfur battery, Mater. Chem. Phys. 255 (2020) 123484, https://doi.org/10.1016/j.matchemphys.2020.123484.

[80] V. Marangon, D. Di Lecce, F. Orsatti, D.J.L. Brett, P.R. Shearing, J. Hassoun, Investigating high-performance sulfur-metal nanocomposites for lithium batteries, Sustain. Energy Fuels 4 (2020) 2907–2923, https://doi.org/10.1039/d0se00134a.

[81] H. Raza, S. Bai, J. Cheng, S. Majumder, H. Zhu, Q. Liu, G. Zheng, X. Li, G. Chen, Li-S batteries: challenges, achievements and opportunities, Electrochem. Energy Rev. 6 (2023) 29, https://doi.org/10.1007/s41918-023-00188-4.

[82] I. Marri, Z. Edfouf, A. Caballero, A.Y. Tesio, Valorisation of argan seeds: production of cathode material for high-performance lithium-sulfur batteries, J. Energy Storage 82 (2024) 110518, https://doi.org/10.1016/j.est.2024.110518.

[83] Z. Wang, B. Wang, Y. Yang, Y. Cui, Z. Wang, B. Chen, G. Qian, Mixed-metal-organic framework with effective Lewis acidic sites for sulfur confinement in high-performance lithium-sulfur batteries, ACS Appl. Mater. Interfaces 7 (2015) 20999–21004, https://doi.org/10.1021/acsami.5b07024.

[84] C.Y.J. Lim, Z.W. Seh, Quasi-solid-state conversion cathode materials for room-temperature sodium–sulfur batteries, Batter. Energy. 1 (2022) 20220008, https://doi.org/10.1002/bte2.20220008.

[85] H. Liu, W.-H. Lai, Q. Yang, Y. Lei, C. Wu, N. Wang, Y.-X. Wang, S.-L. Chou, H. K. Liu, S.X. Dou, Understanding sulfur redox mechanisms in different electrolytes for room-temperature Na–S batteries, Nano-Micro Lett. 13 (2021) 121, https://doi.org/10.1007/s40820-021-00648-w.